

ARTICLE OPEN



Galvanic corrosion behavior of welded joint in marine atmosphere environment based on capillary microcell

Xinyu Wang^{1,2}, Feng Huang^{1,2} , Qian Hu^{1,2}, Jiawei Zhang^{1,2} and Jing Liu^{1,2}

The kinetical behavior and mechanism of micro-galvanic corrosion of Q690 bainitic weathering steel welded joint in marine atmosphere were investigated. The results showed that a micro-galvanic corrosion cell formed among different regions of the Q690 welded joint. The kinetical behavior of micro-galvanic corrosion could be divided into four stages: the initiation and development of micro-galvanic corrosion, the decreasing of galvanic corrosion rate, the polarity reversal of galvanic couple, and the disappearance of galvanic effect. The difference of corrosion rate between Q690 steel and its welded joint is closely related to the micro-galvanic corrosion kinetic behavior.

npj Materials Degradation (2024)8:1 ; <https://doi.org/10.1038/s41529-023-00417-7>

INTRODUCTION

Bridge steel has become a widely used steel after years of development. With the rapid development of social progress and bridge technology, higher requirements have been put forward for bridge steel, i.e., high strength, good corrosion resistance and welding performance, especially in the harsh marine environment. However, the microstructure of steel welded joints is often affected by the welding thermal cycling, resulting in a significant change compared with that before welding¹, thus becoming the weak link of corrosion², especially the local corrosion dominated by galvanic corrosion^{3–5} and stress corrosion^{6,7}. The galvanic corrosion is the most common, with a high local corrosion rate and hidden, and a high likelihood of early catastrophic failure.

There are many reports on galvanic corrosion of welded joints of steel structures, mainly focusing on the research of influencing factors, including electrochemical factors (potential difference and polarization ability^{8,9}), geometric factors (cathode-anode area ratio, galvanic distance and spatial position^{8–12}), and environmental factors (temperature, oxygen content, conductivity Ph, etc.^{9,10,13–16}). For the above factors, researchers have tried a variety of quantitative and qualitative testing methods for different macroscopic galvanic corrosion, such as weight loss measurement, morphology observation, and traditional electrochemical measurement technology^{17–19}. However, with the continuous development of various new technologies, various micro-zone testing methods have been employed to study the micro-galvanic corrosion, which can be induced by the difference in microstructure between the micro-regions, such as base metal (BM), heat-affected zone (HAZ) and weld metal (WM). Wu et al.²⁰ detected the high and low potential areas on the surface of traditional and new 3% Ni weathering steel by scanning Kelvin probe (SKP). Li et al.²¹ simulated the welded joint according to the composition and area ratio by using the array electrode technology, and studied its initial corrosion behavior. Wint et al. measured¹ the current density distribution in the laser-welded joints of high-strength low alloy (HSLA) and hot stamping ultra-high strength steel (UHSS), and comparatively studied the galvanic corrosion behavior by employing scanning vibrating electrode technique (SVET). In our previous work²², the Volta potential distribution of A710 steel welded joints was

determined by SKP to investigate the corrosion thermodynamic behavior of each micro-region of welded joints. However, conventional micro-electrochemical methods such as SKP, SVET, etc., could only give the surface potential or current distribution through the electrical signal between the probe and the metal surface, the electrochemical polarization behavior of each micro-region still cannot be obtained through the above technologies.

The self-designed three-electrode capillary micro-cell can accurately locate the tested micro-region by adjusting the capillary port diameter, thereby obtaining the potentiodynamic polarization curves, and then study polarization behaviors of different micro-regions of the welded joint. Therefore, the technology can overcome the current technical deficiencies and provide a great help for deeply studying the electrochemical mechanism of galvanic corrosion in the micro-regions of welded joint³. Recently, our group improved the structure of capillary microcell, optimized the preparation parameters of Ag / AgCl reference electrode²³, and used it to study the mechanism of inclusion-induced pitting initiation in stainless steel^{22,24}.

In the paper, the 3.5% NaCl was used to simulate the marine atmospheric environment. The surface electrochemical activity and galvanic current of the welded joint of the new generation Q690 bainitic weathering bridge steel were studied by employing SKP, Scanning Reference Electrode Technology (SRET), Zero Resistance Current Meter and self-designed capillary microelectrode technique. At the same time, combining with Raman spectroscopy, field emission electron probe microanalysis (FE-EPMA) and other characterization techniques, and the influence law and mechanism of micro-galvanic corrosion on the corrosion kinetics behavior of the whole welded joint would be clarified, which can provide theoretical basis and data support for the service safety and protection of 690 MPa high strength bainitic weathering steel in simulated marine atmospheric environment.

METHODS

Material preparation

The Q690 high-strength weathering steel used in this research was supplied by Wuhan Iron and Steel Corporation, and the welded joints was obtained using a gas-shielded arc process. The chemical

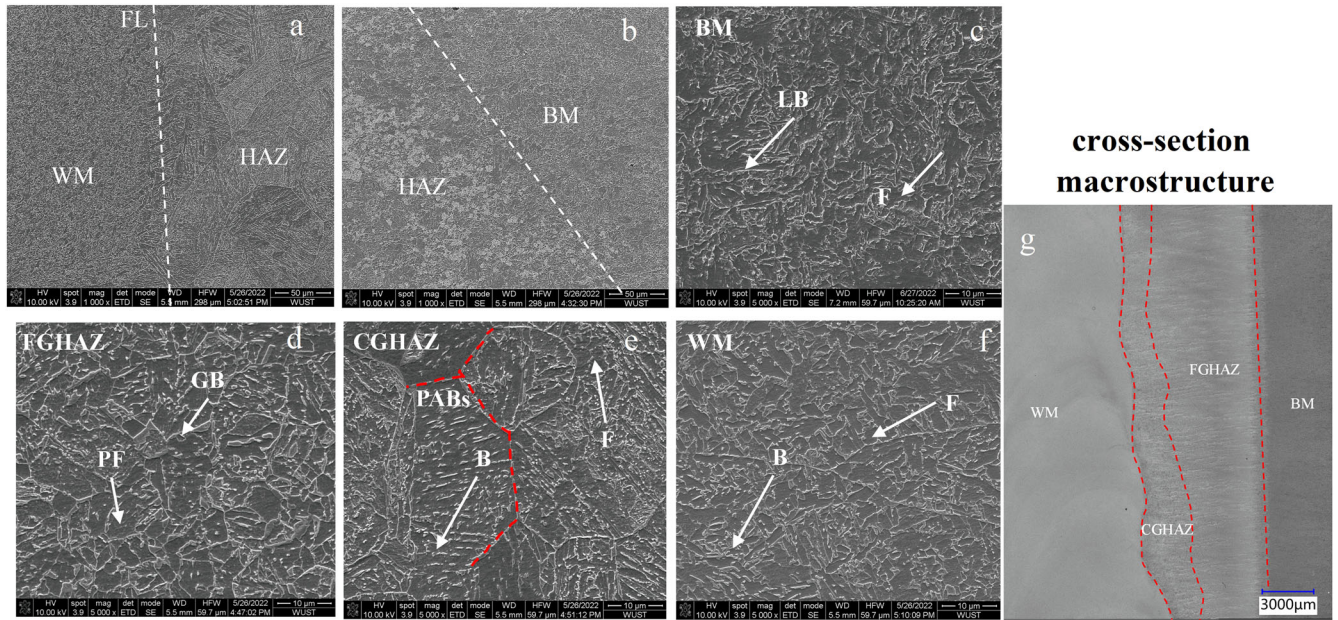
¹The State Key Laboratory of Refractories and Metallurgy, Wuhan University of Science and Technology, 430081 Wuhan, Hubei, China. ²Hubei Engineering Technology Research Centre of Marine Materials and Service Safety, Wuhan University of Science and Technology, 430081 Wuhan, Hubei, China. ✉email: huangfeng@wust.edu.cn

Table 1. Chemical composition of base metal and welding wire (wt. %).

	C	Si	Mn	P	S	Cr	Ni	Cu	Mo	Fe
Q690	0.06	0.21	1.78	0.006	≤0.005	≤0.6	≤0.3	≤0.4	/	Bal.
XY-ER80QNH	≤0.1	≤0.65	≤2.00	≤0.015	≤0.015	≤0.4	≤1.62	≤0.25	≤0.60	Bal.

Table 2. Gas shielded welding process parameters.

Welding wire	Tensile strength R_m (MPa)	Yield strength $R_{p0.2}$ (MPa)	Elongation A (%)	Protective gas
XY-ER80QNH	≤280	≤28	≤30	80%Ar+20%CO ₂

**Fig. 1** FE-SEM images of the microstructure of Q690 welded joint. **a** The junction of WM and HAZ, **(b)** The junction of BM and HAZ, **(c)** BM, **(d)** FGHAZ, **(e)** CGHAZ, **(f)** WM, and **(g)** Q690 welded joint.

composition of the base metal and the welding wire were shown in Table 1. And the welding parameters was shown in Table 2.

Fig. 1 shows the microstructure of the welded joints of 690 bainite weathering steel. It is seen that the base metal (BM) is primarily composed of lath bainite (LB) and a small amount of ferrite (F), and the microstructure is relatively uniform (Fig. 1c). The fine grain heat affected zone (FGHAZ) mainly consists of polygonal ferrite (PF) and granular bainite (GB), with different grain sizes (Fig. 1d). The coarse grain heat affected zone (CGHAZ) (Fig. 1e) has coarse grains, and a large number of primary austenite boundaries (PABs) are observed (red dotted line in Fig. 1e), the microstructure is mainly composed of bainite and ferrite. The weld metal (WM) is mainly composed of non-uniform bainite and ferrite with coarse grains. Fig. 1g is the cross-sectional morphologies on welded joints which present various areas. There are significant differences in the grain size and microstructure in the different regions of the welded joint, which would result in the difference in the electrochemical activity between the different regions, and then initiating the galvanic effect between different regions^{25–27}.

Wet/dry alternating corrosion test

The wet/dry alternating corrosion test was conducted to investigate corrosion of Q690 welded joint steels in simulated marine atmospheric environments according to standard GB/T 19746 – 2018²⁸.

The total duration of the test was 576 h, and sampling was performed at 24 h, 48 h, 72 h, 96 h, 192 h and 576 h. Seven specimens were used for each type of steels for reproducibility of the results, where five parallel specimens (60 × 40 × 5 mm in dimension) were used for weight-loss testing, one (20 × 15 × 5 mm) was used for Raman analysis, one (20 × 15 × 5 mm) was used for morphological and elemental analysis by FE-EPMA. The test solution was 3.5 wt.% NaCl solution. The temperature in the test chamber during the drying period was (45 ± 2) °C, and the relative humidity was (70 ± 2) %. Each dry/wet cycle was 60 min, with a drying time of 48 min and an infiltration time of 12 min.

After wet/dry alternating corrosion test, the specimens used for weight-loss testing were ultrasonically cleaned in a descaling solution (500 mL hydrochloric acid + 500 mL distilled water + 3.5 g hexamethylenetetramine), and then washed with absolute ethanol, dried in high-purity nitrogen (99.999%) and weighed by a balance (m_t) with an accuracy of 0.1 mg. To determine the error caused by dissolution of the steel specimen in the descaling solution, a blank specimen (without corrosion test) of the same size was used for weight-loss correction in the descaling process. The blank specimen was placed in the etching solution with the same time, and the weight loss was recorded as m_1 . The corrosion rate was calculated by:

$$V_a = \frac{m_0 - m_t - m_1}{St} \quad (1)$$

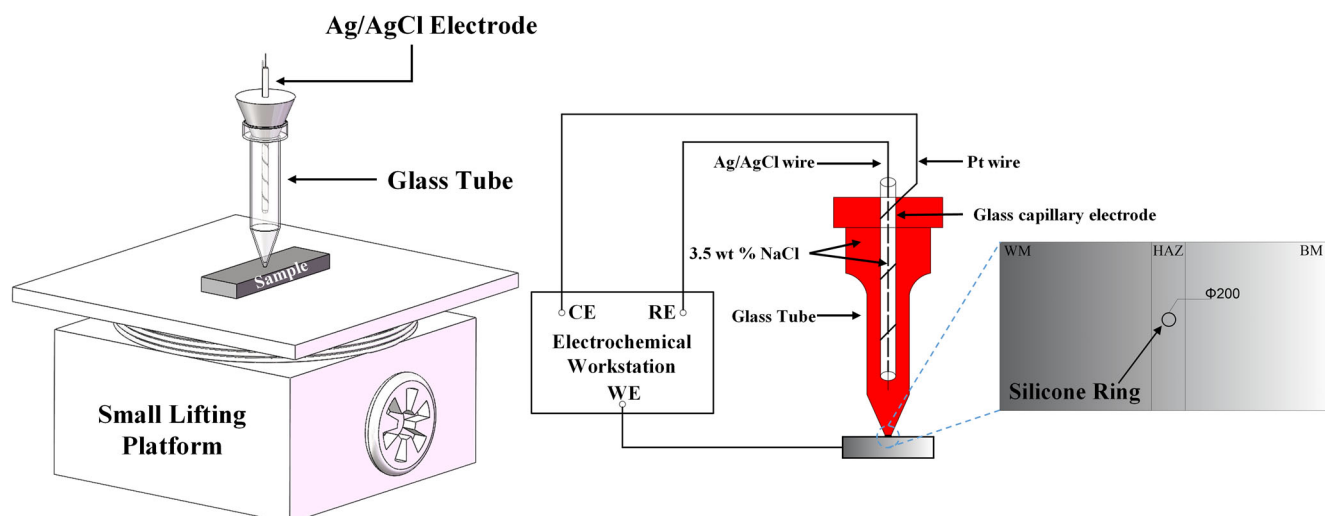


Fig. 2 Self-designed capillary micro-cell test device schematic diagram. 3D schematic and 2D schematic of the device.

where V_a is the average corrosion rate ($\text{g m}^{-2} \text{h}^{-1}$), S is the sample area (m^2), t is time(h), m_0 is the initial weight of the specimen, m_t is the weight loss of the specimen, m_i is the weight loss of blank specimen.

SKP test

The Volta potential distributions for different regions of the Q690 weathering steel welded joints were measured using a VersaSCAN electrochemical workstation with the SKP technique with a size of $50 \times 10 \text{ mm}$ scanned area, a $100 \mu\text{m s}^{-1}$ scanning step at room temperature ($\sim 25^\circ\text{C}$) and a relative humidity of 40%. A tungsten wire probe with a diameter of $100 \mu\text{m}$ was invoked as the needle, whose amplitude and frequency were $30 \mu\text{m}$ and 1 kHz , respectively. And the average distance between the sample surface and the Kelvin probe was approximately $100 \mu\text{m}$ during the testing. The welded joint specimens were wet ground with silicon carbide papers up to 2000 grit, and then polished with diamond suspensions (size of $3 \mu\text{m}$). After that, the specimen was etched slightly with 4% nital (4 mL nitric acid + 96 mL ethyl alcohol) to distinguish the BM, HAZ and WM regions of the welded joint.

SRET test

The surface current distribution of the welded joint during corrosion was measured by XMU-BY-LG scanning electrochemical workstation with a scanning size of $20 \text{ mm} \times 10 \text{ mm}$. The sample was first etched to show the three regions according to the experimental steps described in 2.3, and the boundary of each region was marked and then the sample was re-polished. According to the previous marker, the scanning area was selected to include BM, HAZ and WM.

Micro-electrochemical measurements

The electrochemical polarization behavior of different regions of Q690 steel welded joint was studied using a self-designed capillary microcell, as shown in Fig. 2. The steel sample is used as the working electrode (WE), and the Ag / AgCl wire in the glass capillary as the reference electrode (RE), the platinum wire wrapped outside the glass capillary as the counter electrode (CE), in other words, RE and CE is isolated and insulated by the glass capillary in the glass tube filled with corrosive media. The circular ring with a diameter of $\Phi 200$ is a glass tube mouth, and the surface is coated with a silicone ring. Moreover, each micro-area electrolytic cell is isolated and insulated from other micro-areas due to corrosive media, which is just in the area to be tested. The linear polarization scanning range was $\pm 10 \text{ mV}$ (vs OCP) and the

scanning rate was 0.25 mV s^{-1} . The frequency range of electrochemical impedance was $10^{-2} \sim 10^5 \text{ Hz}$, and the amplitude of AC excitation signal was 10 mV , and the temperature was $25 \pm 2^\circ\text{C}$.

Galvanic current measurement in different regions of welded joints

Fig. 3 shows the schematic diagram of the galvanic couple current measurement between different regions of Q690 steel welded joint. In the dry / wet cycle accelerated corrosion testing, the CST500(ZRA) was used to continuously measure the galvanic current in different regions of the Q690 steel welded joint. The different parts of the Q690 welded joint were divided, and the BM was used as the working electrode 1. In the galvanic current measurement device, the HAZ + WM used he working electrode II. If the current measured by CST500 is positive, the working electrode I is the anode; on the contrary, the working electrode II is the anode. The size of electrode 1 (BM) was $28 \times 20 \text{ mm}$ and the size of electrode 2 (HAZ + WM) was $26.7 \times 20 \text{ mm}$. In addition, it is worth emphasizing that the area ratio of BM, HAZ and WM was the same as that in the dry/wet accelerated corrosion cycle testing, and the measurement would be stopped until the galvanic current approached zero.

Morphological and element composition characterization

The morphologies of the steel specimens after dry/wet alternating corrosion testing for various times were observed using a digital camera (LEICAVARIO-SUMMILUX-H). After the test was completed, the specimens were sealed in epoxy resin. The cross-sectional morphology of the corroded specimen was characterized by FE-EPMA-8050G with an acceleration voltage of 15 kV , irradiation current of 100 nA , and beam diameter of $1 \mu\text{m}$.

Raman spectroscopy (Renishaw, inVia Qontor, England) was used to determine the composition of the corrosion products, with the laser wavelength of 532 nm , the power of 50 mW and the exposure time of 10 s . The scanning range was within $0 \sim 1800 \text{ cm}^{-1}$, with a linear scan range of $200 \mu\text{m}$ and a sampling dimension of 1 point per $90 \mu\text{m}$. The results were analyzed using NanoScope Analysis 2.0 software.

RESULTS

Volta potential distribution of Q690 steel welded joint

The Volta potential distribution of the Q690 welded joint measured via Kelvin probe is shown in Fig. 4. From Fig. 4b, it is seen that the potential for different regions of the Q690 welded

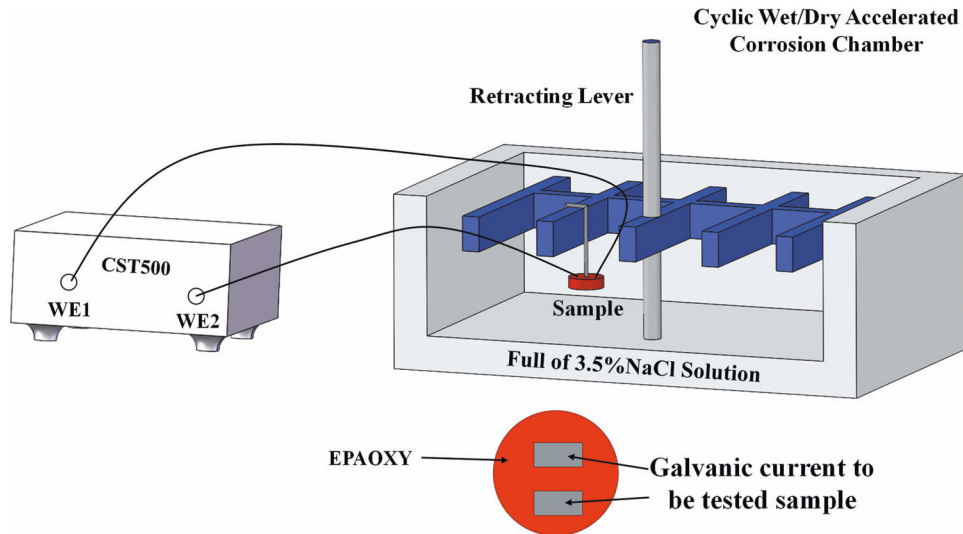


Fig. 3 The schematic diagram of galvanic couple current measurement in different regions of welded joint under wet/dry alternating environment. These are the schematic diagrams of the detection device, periodic infiltration device, and sample for detection.

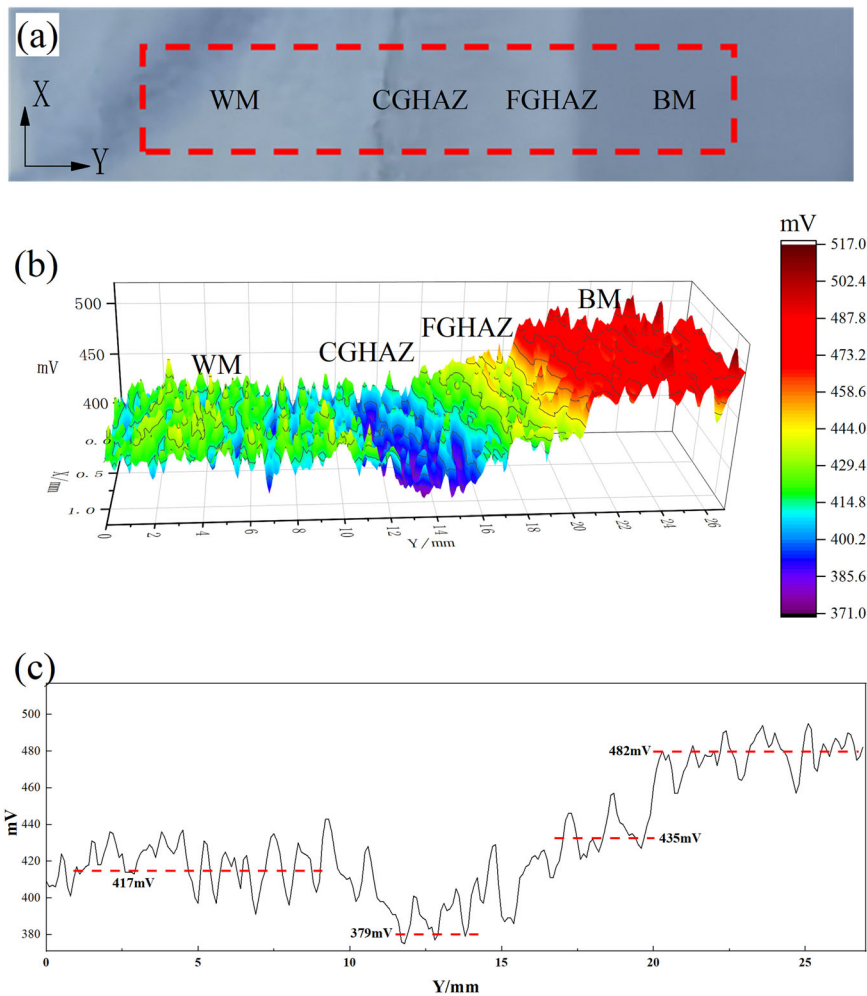


Fig. 4 Volta potential distribution in different regions of Q690 welded joint. **a** SKP macro testing area; **b** SKP 3D view; **c** SKP line distribution map.

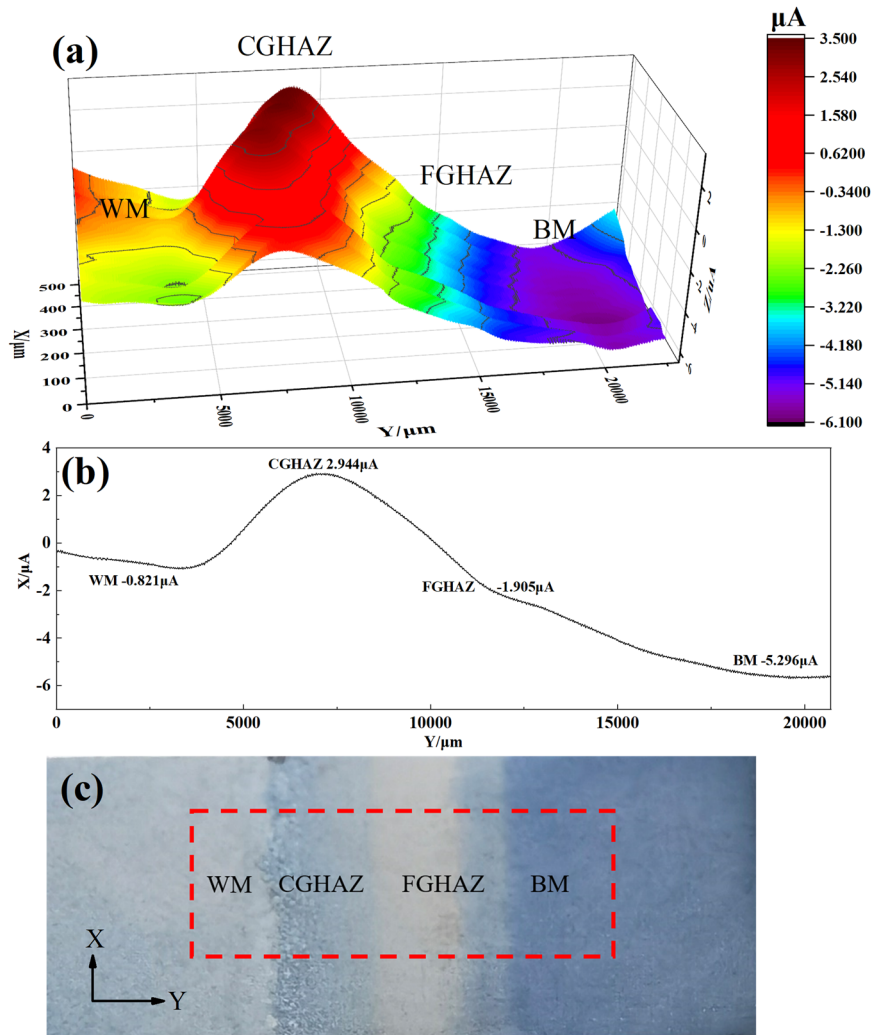


Fig. 5 Ampere SRET diagram of Q690 steel welded joint in different micro regions. **a** 3D figure; **(b)** Line distribution map; **(c)** SRET macro testing area.

joint progressively decreases in the order of BM, FGHAZ, WM and CGHAZ, and the maximum potential difference between these regions exceeds 100 mV, reaching the electrochemical conditions for galvanic corrosion²⁹.

M · Stratmann³⁰ proved that the self-corrosion potential E_{corr} of the metal had the following relationship with the volta potential $\Delta \Phi$ measured by the scanning Kelvin probe test :

$$E_{corr} = \Delta \Phi + Const \quad (2)$$

where $Const$ is the constant determined by the experiment.

Therefore, according to the measured volta potentials, the order of the Volta potentials of the different regions in the welded joint could be judged as follows: BM (482 mV) > FGHAZ (435 mV) > WM (417 mV) > CGHAZ (379 mV). The large potential difference in the different regions indicates that there may be galvanic corrosion for the Q690 steel welded joint in the harsh marine atmospheric corrosion environment.

Surface current distribution of Q690 steel welded joint

Figure 5 gives the surface current distribution of Q690 steel welded joint in 0.01 wt % NaCl solution. An anodic current of about 2.944 μA is observed on CGHAZ, which is higher than those of other regions, while a cathodic current of about $-5.296 \mu\text{A}$ is observed on BM. The higher anodic current means that the

CGHAZ had higher electrochemical activity, which acts as the anode of the micro-region galvanic corrosion cell. This is consistent with the testing results of SKP.

Corrosion kinetics of Q690 steel and its welded joint under cyclic immersion test

Figure 6 shows the average corrosion weight loss rate of Q690 steel base metal and welded joint after the wet/dry alternating test. It is seen that both the corrosion rates of Q690 base metal and welded joint increase firstly (24h–72h), and then reaches the maximum at 72 h, and then gradually decreases. Comparing these two corrosion rates, it can be found that the corrosion rate of welded joint is larger than that of base metal, indicating that the corrosion resistance of welded joint is worse than that of base metal. The dotted line in Fig. 6 indicates the corrosion rate difference between the base metal and welded joint. It could be seen that with the increase of immersion time, the corrosion rate difference increases first and then decreases, reaching the maximum on the 6th day ($0.2874 \text{ g m}^{-2} \text{ h}^{-1}$).

The double logarithmic model is usually used to study the atmospheric corrosion kinetics of metal materials³¹:

$$\lg(C) = n \lg(t) + \lg(A) \quad (3)$$

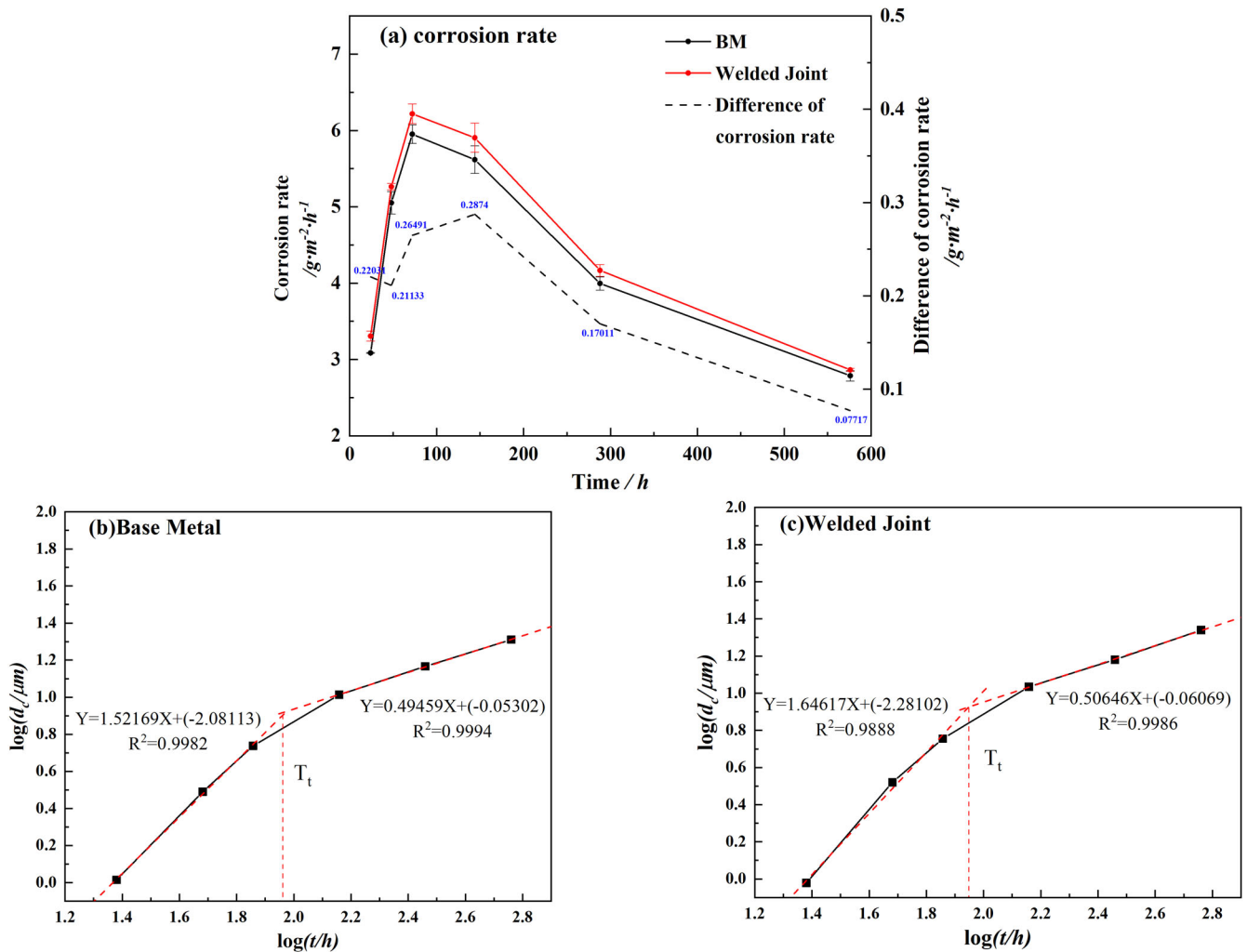


Fig. 6 The average corrosion weight loss rate of Q690 steel base metal and welded joint after the wet/dry alternating test. Corrosion kinetics curves (a), corrosion depth-time double logarithmic curve of Q690 steel (b), and its welded joint (c) under wet/dry cycle accelerated corrosion test.

where C is the reduction in thickness (μm) of metal material; t is the corrosion time (h). A and n are constants.

The double logarithmic model was employed to explore the corrosion kinetics of Q690 steel base metal and its welded joint with the measured weight loss corrosion rate, as shown in Fig. 6(b, c). The n value in Eq. (1) could reflect the characteristic of the corrosion kinetics. $n < 1$ means a declined corrosion process, and $n > 1$ means an accelerated corrosion process, while $n = 1$ means a constant corrosion process. The n value transfers from $n > 1$ to $n < 1$ between 72h–96h, which is consistent with the change of corrosion rate with time in Fig. 6a. In general, the greater the n value, the greater the corrosion trend³². In the initial stage of corrosion, the n value of the base metal and the welded joint is quite different ($\Delta n = 0.12$), but Δn decreases to 0.01 after 72 h. Therefore, the difference in corrosion rate between Q690 steel base metal and its welded joint decreases after forming a stable rust layer in the later stage of corrosion.

The surface macro morphology of Q690 base metal and welded joint before and after removal of corrosion products

Fig. 7 shows the macroscopic morphology of Q690 base metal and welded joint before and after rust removal in different corrosion cycles. With the increase of corrosion time, the rust layers on base

metal and welded joint are composed of two layers of corrosion products: reddish brown outer layer and black inner layer, and gradually becomes dense (Fig. 7a). After removing the rust layer, the surface morphology of base metal after different corrosion cycles is almost the same, showing uniform corrosion characteristics (Fig. 7b). While for the welded joint, the samples emerge different degrees of groove-like corrosion morphology in the weld area after removing the rust layer, and the corrosion groove gradually becomes obvious (Fig. 7b).

Cross-section morphology and element distribution of the rust layer

The cross-sectional morphology and the element distribution of the rust layers of Q690 base metal and welded joint after corrosion for 24 days are shown in Fig. 8. It could be seen that both the rust layers of BM and WM are composed of inner and outer layers. The overall thicknesses of the rust layers of BM and WM are about 530 μm and 580 μm , respectively. There is not much different in the thickness of the inner rust layer, but the cavities and cracks in the BM rust layer are less than those in the WM rust layer, and the rust layer of BM is denser. In addition, Cr, Si, and Cu elements are enriched in the inner rust layer, and Cu and Cr are enriched in the inner rust layer near the substrate side. Furthermore, the

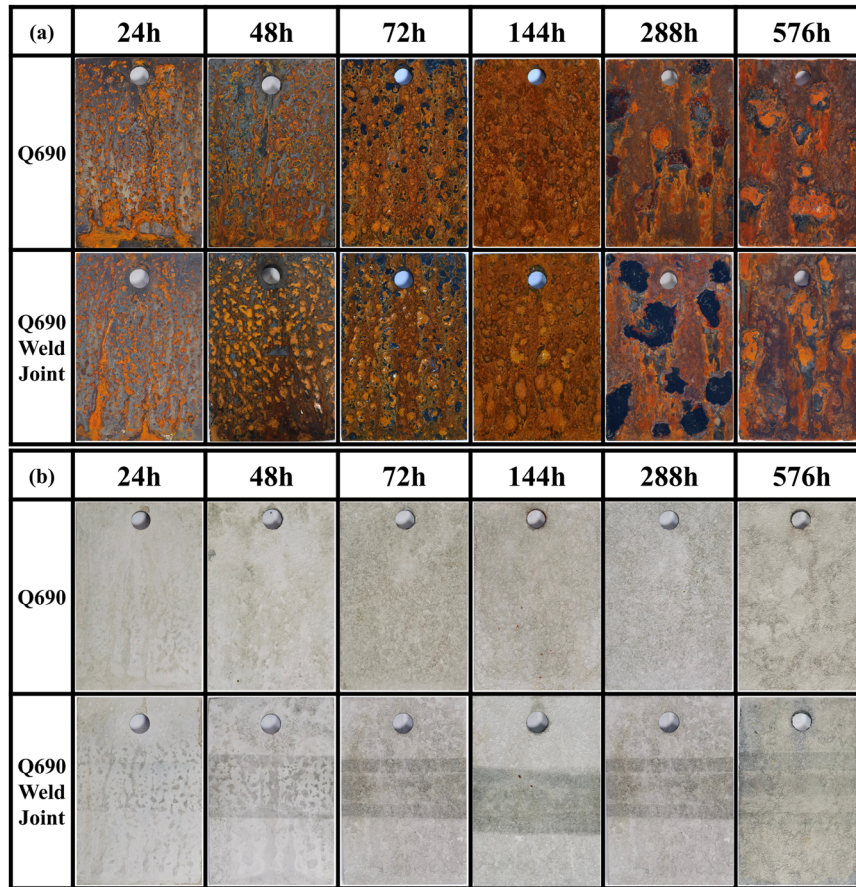


Fig. 7 The macroscopic morphology of Q690 steel and its welded joint. The macroscopic surface morphology of Q690 steel and its welded joint samples before (a) and after (b) removal of corrosion products as a function of test time.

enrichment degree of Si, Cr, and Cu elements in BM rust layer is higher than that in WM rust layer, which should be relationship to the higher content of these elements in the base metal³³. And our previous research also found that the Si content in steel around 0.2 wt.% had a better protective effect on the rust layer³⁴.

Raman spectrometer analysis of the rust layers of Q690 steel base metal and welded joint

The Raman spectra of the rust layers formed on the Q690 steel and welded joint are shown in Fig. 9. It can be seen from Fig. 9 that there is no difference in the chemical composition of the inner and outer rust layers between BM and WM, which are composed of α -FeOOH, γ -FeOOH and Fe_3O_4 . The position of the main peak corresponding to α -FeOOH is at around 387 cm^{-1} ^{20,35}. It is worth noting that the intensity of α -FeOOH peak in BM inner rust layer is higher, which indicates that the content of α -FeOOH in BM inner rust layer is higher. Especially at point 1, the enrichment of Cr element can promote the transformation of α -FeOOH in the rust layer³³. In addition, the enrichment of Si result in the formation of a stable amorphous SiO_2 with a three-dimensional network structure in the rust layers promoting the formation of α -FeOOH³⁴.

Electrochemical corrosion behavior of different micro-regions in Q690 steel welded joint

From the above experimental results, it is seen that macroscopic galvanic corrosion could occur on the Q690 steel welded joint in the marine atmospheric environment. In order to further clarify its

galvanic corrosion mechanism, the electrochemical corrosion behavior of different regions of Q690 steel welded joint was measured by self-designed capillary microcell.

Micro-regions corrosion potential measurement. Figure 10 shows the variation curve of open circuit potential with time in three different regions (base metal, heat affected zone, and weld metal) of Q690 steel welded joint. It could be seen from Fig. 10 that the open circuit potentials of the three different regions of the Q690 steel welded joint gradually decline until stable. The order of stable open circuit potentials in the three different regions is: BM (-0.474 V) > FGHAZ (-0.515 V) > WM (-0.526 V) > CGHAZ (-0.538 V). The large potential difference between BM and CGHAZ indicates that the CGHAZ has a greater corrosion tendency than the other regions³⁶, and the overall welded joint is more susceptible to galvanic corrosion.

Micro-regions linear polarization (LP) measurement. The polarization resistance R_p could reflect the corrosion rate of metal to a certain extent³⁷. A large R_p value indicates the high corrosion resistance of the steel. The linear polarization curves of the different regions in Q690 steel welded joint are shown in Fig. 11. The fitted polarization resistance R_p values are: BM ($2163.55\Omega\text{ cm}^{-2}$) > FGHAZ ($1705.51\Omega\text{ cm}^{-2}$) > WM ($1284.9\Omega\text{ cm}^{-2}$) > CGHAZ ($960.38\Omega\text{ cm}^{-2}$), which indicates that BM has the best corrosion resistance, while CGHAZ has the worst corrosion resistance.

Micro-regions electrochemical impedance spectroscopy measurement. Electrochemical impedance spectroscopy (EIS) is one of

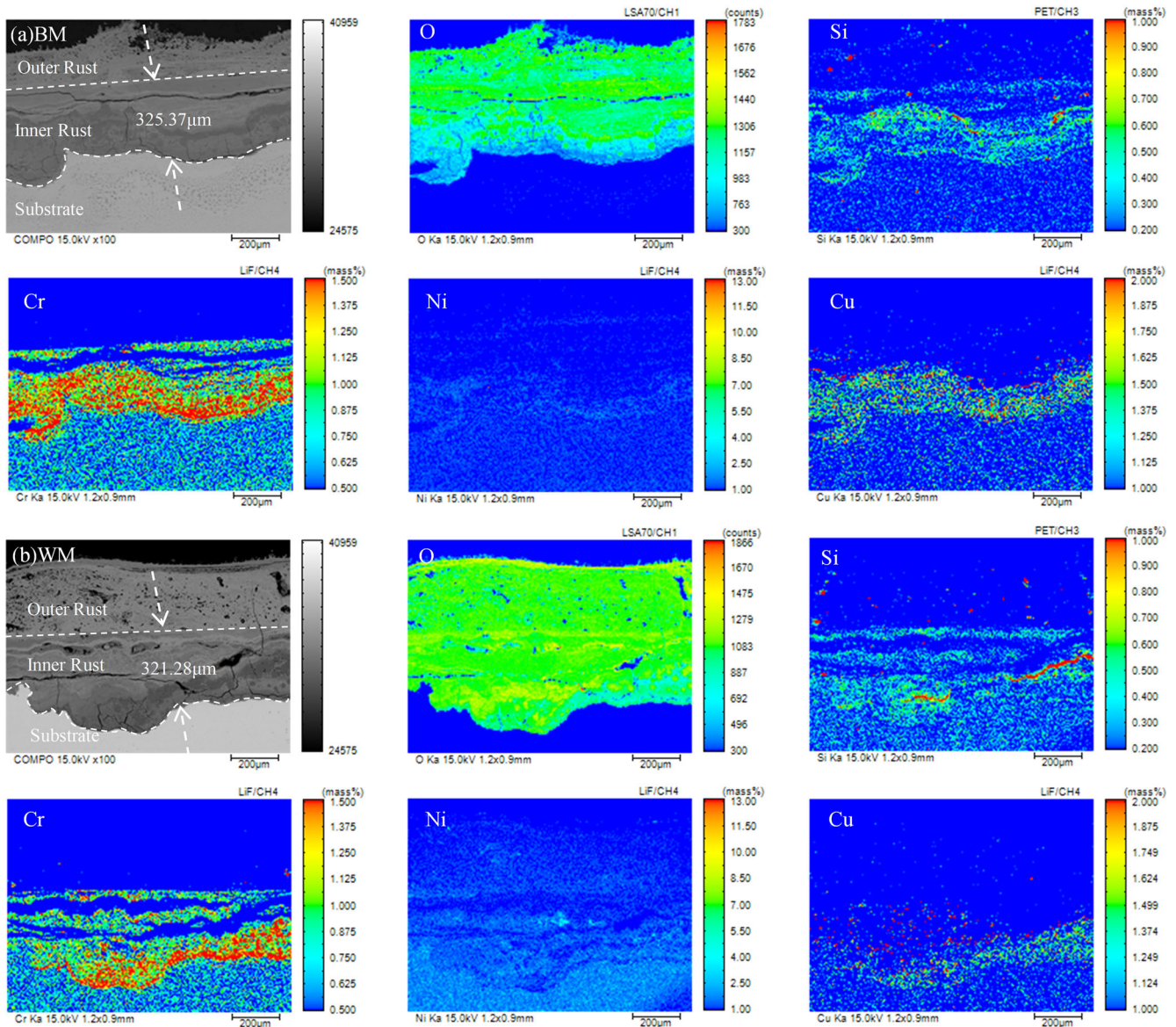


Fig. 8 Section and element distribution of rust layer of Q690 steel base metal and welded joint. **a** BM rust layer, **(b)**WM rust layer.

the effective methods to study the corrosion resistance of steel^{38,39}. Figure 12 shows the Nyquist and Bode diagrams of the four regions (BM, FGHAZ, CGHAZ, and WM). It is seen that the impedance spectra of the four regions emerge as an extended semicircle (Fig. 14a).

In order to quantitatively analyze the corrosion resistance of the four regions of Q690 steel welded joint, the EIS were fitted with the equivalent circuit in Fig. 14a. The fitting results are shown in Table 3. The CPE-Y and CPE-n are a parameter related to capacitance and exponential term related to roughness of electrode surface, respectively. Notably, the Y values for CGHAZ, WM, FGHAZ and BM exhibit an upward trend, indicating a gradual loosening of the corrosion product films⁴⁰. The electrode/solution transfer resistance R_{ct} in Nyquist diagram, which reflects the difficulty of charge transfer at the electrode / solution interface during corrosion, is in the order: $R_{ct}(\text{BM}) > R_{ct}(\text{FGHAZ}) > R_{ct}(\text{WM}) > R_{ct}(\text{CGHAZ})$. Meanwhile, the evolution of $|Z|_{0.01\text{Hz}}$ used for qualitatively characterize the protectiveness of the rust film exhibits a consistent result in the corresponding Bode diagram. Therefore, the corrosion resistance of BM is the best, and the surface activity of the CGHAZ is

highest (worst corrosion resistance), which is consistent with the linear polarization results.

Galvanic corrosion between different regions in Q690 welded joint

From the electrochemical measurement of each region in the Q690 welded joint (Figs. 10–12), it can be seen that the surface electrochemical activity of BM is quite different from the other three regions. Combined with the surface volta potential (Fig. 4) and current distribution (Fig. 5), it could be preliminarily inferred that in the early stage of corrosion, BM is inclined to be protected in galvanic corrosion, while the corrosion of HAZ (FGHAZ and CGHAZ) is inclined to be accelerated, especially for CGHAZ. Therefore, there may be galvanic corrosion between the local regions of Q690 steel welded joint.

To intuitively and quantitatively analyze the galvanic corrosion behavior of Q690 steel welded joint, the galvanic current between the BM and HAZ + WM couples was measured, as shown in Fig. 13. In each dry/wet cycle, there are current fluctuations during alternate dry/wet cycles, and no current is

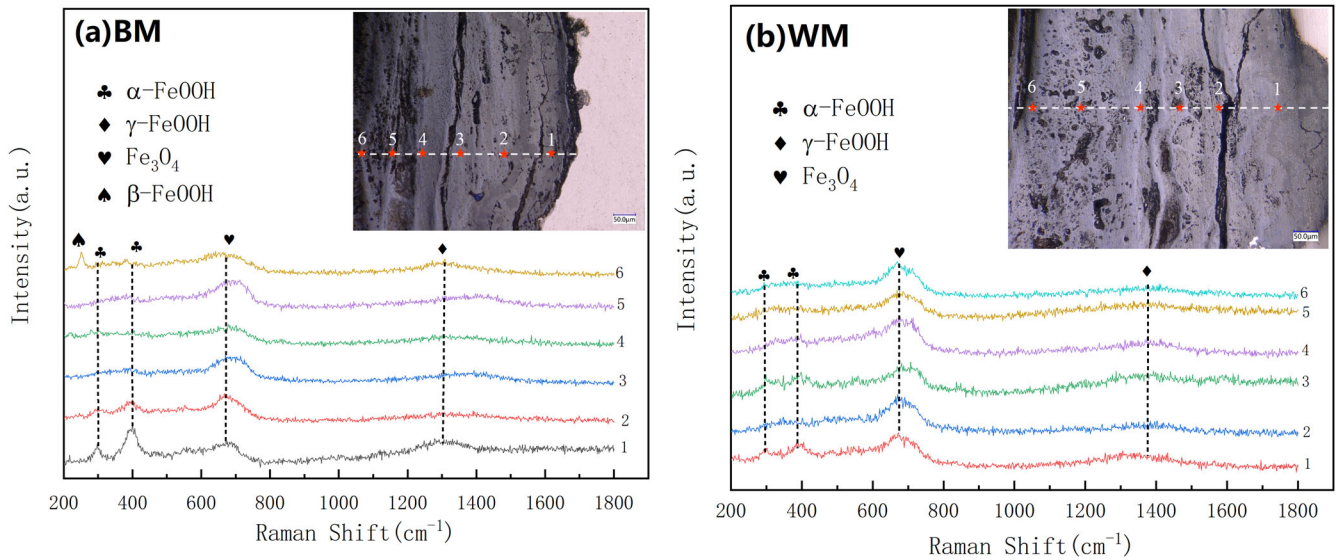


Fig. 9 Raman spectrometer of the rust layers. Raman spectrometer line distribution of rust layer cross section of Q690 steel (a) BM and (b) WM samples.

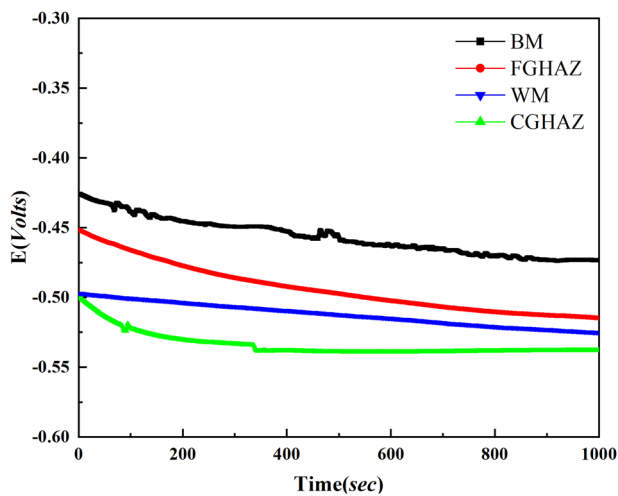


Fig. 10 Open circuit potential of different micro-regions of Q690 welded joint. The open circuit potentials of different regions in the welded joint of Q690 steel are represented using different colors.

displayed during the 48 min of drying period of each cycle. In addition, if the measured current is positive, the working electrode I (WM + HAZ) is the anode. It can be seen from Fig. 13 that a positive galvanic current is present in the initial stage of corrosion, which indicates that the WM + HAZ acts as anode and BM acts as cathode. By calculating the average value of the galvanic current in the immersion stage of each cycle, the variation of the galvanic current with time can be quantitatively analyzed. As shown in in Fig. 14, the change of galvanic current of Q690 welded joint under dry/wet cycle conditions can be obviously divided into four stages: (I) initiation stage; (II) development stage; (III) polarity reversal inversion stage; (IV) galvanic effect disappearance stage. Correspondingly, the galvanic current first rises, and reaches the highest value of 0.00256 A/cm^2 , and then gradually decreases to zero, and finally the polarity is reversed. The negative galvanic current also increases first and then gradually decreases to zero.

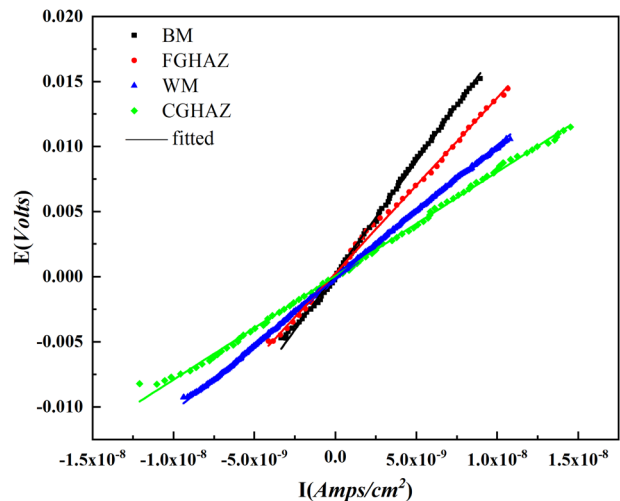


Fig. 11 Linear polarization curves of different micro-regions of Q690 welded joint. The linear polarization curves of different regions in the welded joint of Q690 steel, along with their respective fitting curves, are represented using different colors.

DISCUSSION

Generally speaking, the microstructure has a great influence on the corrosion resistance of weathering steel before the formation of rust layer⁴¹. The Q690 bainitic weathering steel welded joint in this study has different electrochemical activities in different regions (BM, HAZ, WM) due to the difference in the microstructure in these regions (Fig. 1) (Figs 4–5, Fig. 10). Then the corrosion behavior in different regions is significantly different (Figs 10–12), which leads to the occurrence of galvanic corrosion between different regions (Fig. 13).

Fig. 15 shows the four-stage diagram of the evolution mechanism of the galvanic corrosion of the Q690 steel welded joint in the marine atmosphere. In the early stage of galvanic corrosion (before 72 h) (Fig. 15a), the HAZ + WM region with high electrochemical activity acts as the anode of the galvanic corrosion cell to dissolve preferentially, while the BM acts as the

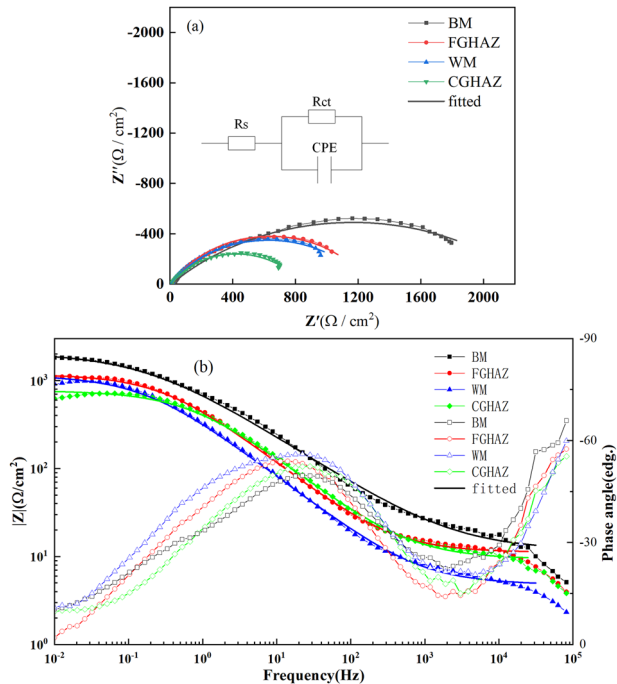


Fig. 12 Electrochemical impedance spectroscopy of different regions of Q690 steel welded joints. **a** Nyquist diagram and equivalent circuit diagram, **b** Bode diagram and phase angle diagram. R_s is solution resistance, R_{ct} is charge transfer resistance, CPE is double charge layer constant phase element.

Table 3. Q690 welded joint fitting results.				
	$R_s/(\Omega\text{-cm}^2)$	$R_{ct}/(\Omega\text{-cm}^2)$	CPE-Y ($10^{-4}\Omega^{-1}\text{cm}^{-2}\text{s}^{\text{CPE-n}}$)	CPE-n
BM	45.02	2316.49	3.436	0.6298
FGHAZ	44.41	1257.39	5.078	0.6924
WM	44.89	1231.87	5.689	0.6912
CGHAZ	44.78	882.95	6.682	0.6844

cathode to be protected. This forms a small anode/large cathode galvanic corrosion cell. (the area of BM in the welded joint is larger than that of WM + HAZ). With the formation of rust layer in the area of WM + HAZ, the area of small anode decreases and the corrosion rate increases. The corrosion of welded joint enters the first stage of galvanic corrosion evolution (Figs 13–14), and corrosion grooves begin to appear in the weld zone accordingly, and gradually deepens (Fig. 7b).

In the middle stage of corrosion (72 h – 144 h), most of WM + HAZ is covered by the rust layer (Fig. 15b). Although the area of the small anode is further reduced, some areas in the BM are also covered by the rust layer, resulting in a decrease in the overall galvanic corrosion rate (Fig. 6. 72 h – 144 h). At this time, the corrosion of welded joint enters the second stage with a declined galvanic current (Fig. 14). Due to the existence of galvanic corrosion, the corrosion of the welded joint is decelerated.

With the further corrosion, the surface of WM + HAZ is covered by corrosion products in the middle and late stages of corrosion (144 h – 288 h), the self-corrosion potential of WM + HAZ shifts positively, which is higher than that of BM, resulting in the polarity reversing of the galvanic corrosion cell, the BM acts the anode and the WM + HAZ acts as the cathode in corrosion couple⁴². Therefore, the corrosion galvanic current also became negative value from the positive value in the previous stage, and entering

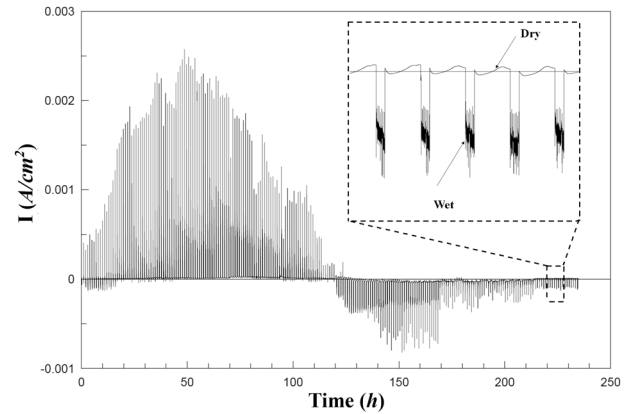


Fig. 13 The change curve of actual galvanic current of Q690 welded joint with time under wet/dry cycle alternation. The real-time monitored galvanic current graph, along with its local magnified view. The galvanic current during the drying stage is around 0.

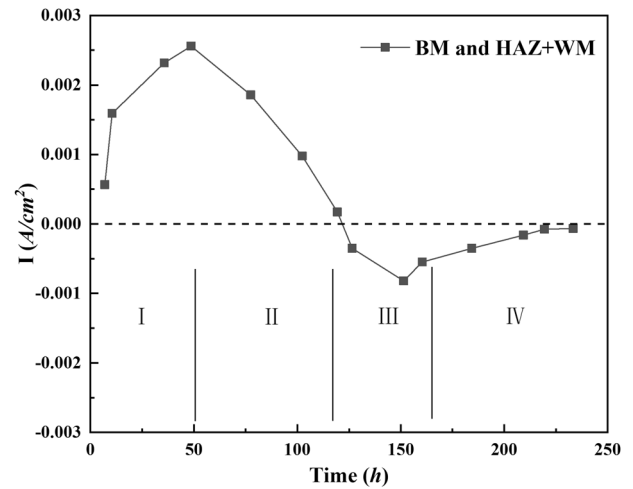


Fig. 14 The variation curve of the average value of the galvanic current of the Q690 welded joint with time under wet/dry cycle alternation. The entire galvanic corrosion process is divided into four stages, designated as I, II, III, and IV in the graph, with the dashed line indicating the zero current level.

the third stage — polarity reversal stage of galvanic corrosion (Fig. 15c).

In the later stage of corrosion (288 h – 576 h), with the extension of dry / wet cycle accelerated corrosion time, all the regions of the galvanic corrosion cell of welded joint are covered by a stable rust layer. The corrosion enters the fourth stage of galvanic corrosion (Fig. 15d). Then the galvanic effect is weakened until it disappears, and the galvanic current approaches to zero (Fig. 14). At this time, the difference in the corrosion rate between the base metal and the welded joint is reduced, the difference in corrosion depth between the different regions is also gradually decreasing, and the corrosion grooves disappear with the time (Fig. 7. 288 h – 576 h). The galvanic effect⁴³, and the corrosion resistance of the welded joint is mainly determined by the protective performance of the rust layer (Fig. 8). In addition, due to the enrichment of Cr, Cu, Si elements and $\alpha\text{-FeOOH}$ which endues the rust layer with good protection, the synergistic effect of these factors could greatly improve the protection ability of the rust layer, so that the corrosion rate difference between the base metal and the welded joint tends to be stable (Fig. 6).

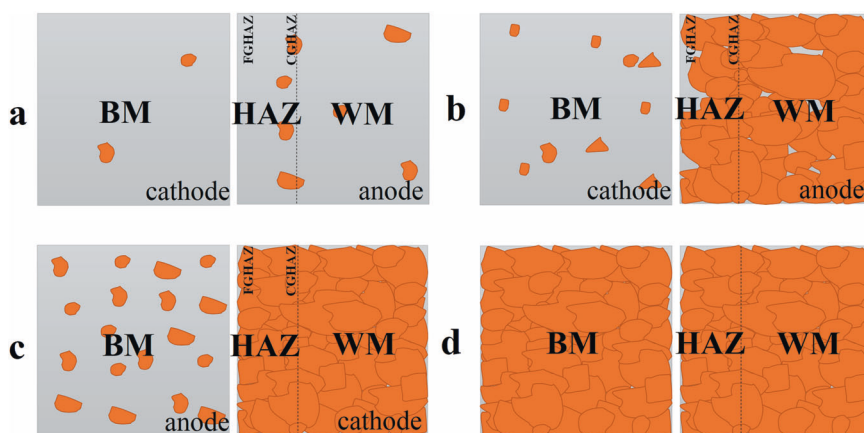


Fig. 15 Mechanism of galvanic corrosion kinetics of Q690 welded joint in marine atmosphere. The **a**, **b**, **c**, and **d** correspond to the four stages (I, II, III, IV) in Figure 14, where the gray-white color represents the steel substrate and the orange-yellow color represents the rust.

In the simulated marine atmospheric environment, the whole corrosion process of Q690 weathering steel welded joint could be divided into two stages: accelerated corrosion and decelerated corrosion. In the same corrosion cycle, the corrosion rate of Q690 welded joint is larger than that of its base metal, and their corrosion rate difference increased first and then decreased until stable with the corrosion time goes by. The corrosion rates of the base metal and welded joint increase first with the galvanic effect, and tend to be stable after the reversal. The more significant the galvanic effect, the greater the difference in the corrosion rate between the base metal and welded joint.

DATA AVAILABILITY

The raw/processed data required to reproduce these findings cannot be shared at this time due to technical or time limitations.

Received: 30 July 2023; Accepted: 12 December 2023;

Published online: 04 January 2024

REFERENCES

1. N. Wint, et al. The galvanic corrosion of welded ultra-high strength steels used for automotive applications. *Corros. Sci.* **136**, 366–373 (2018).
2. Wang, Y. X., Tsutsumi, S., Kawakubo, T. & Fujii, H. Microstructure and mechanical properties of weathering mild steel joined by friction stir welding. *Mater. Sci. Eng. A* **823**, 141715 (2021).
3. Zhu, J. Y. et al. Galvanic corrosion of a welded joint in 3Cr low alloy pipeline steel. *Corros. Sci.* **111**, 391–403 (2016).
4. Lin, Y. J. & Lin, C. S. Galvanic corrosion behavior of friction stir welded AZ31B magnesium alloy and 6N01 aluminum alloy dissimilar joints. *Corros. Sci.* **180**, 109203 (2021).
5. Zhu, G. Y., Li, Y. Y. & Zhang, G. A. Interaction between crevice and galvanic corrosion of X65 carbon steel in the CO₂-saturated NaCl solution under the coupling of crevice and galvanic effects. *J. Electroanal. Chem.* **918**, 116482 (2022).
6. Gao, F. Y. et al. Stress corrosion characteristics of electron beam welded titanium alloys joints in NaCl solution. *Mater. Charact.* **192**, 112126 (2022).
7. Ma, H. C. et al. Stress corrosion cracking of E690 steel as a welded joint in a simulated marine atmosphere containing sulphur dioxide. *Corros. Sci.* **100**, 627–641 (2015).
8. Zhang, D.-L., Wang, W. & Li, Y. An electrode array study of electrochemical inhomogeneity of zinc in zinc/steel couple during galvanic corrosion. *Corros. Sci.* **52**, 1277–1284 (2010).
9. Shi, L. J. et al. Effect of corrosive media on galvanic corrosion of complicated tri-metallic couples of 2024 Al alloy/Q235 mild steel/304 stainless steel. *J. Mater. Sci. Technol.* **35**, 1886–1893 (2019).
10. Fushimi, K., Naganuma, A., Azumi, K. & Kawahara, Y. Current distribution during galvanic corrosion of carbon steel welded with type-309 stainless steel in NaCl solution. *Corros. Sci.* **50**, 903–911 (2008).
11. Jia, J. X., Song, G. & Atrens, A. Experimental measurement and computer simulation of galvanic corrosion of magnesium coupled to steel. *Adv. Eng. Mater.* **9**, 65–74 (2007).
12. Yaro, A. S., Khadom, A. A. & Idan, M. A. Galvanic corrosion inhibition behavior of coupled copper—Steel alloys in cooling water system. *J. Environ. Chem. Eng.* **2**, 2120–2128 (2014).
13. Zhang, G. A., Yu, N., Yang, L. Y. & Guo, X. P. Galvanic corrosion behavior of deposit-covered and uncovered carbon steel. *Corros. Sci.* **86**, 202–212 (2014).
14. Cui, T. F. et al. Effect of NaCl concentration, pH value and tensile stress on the galvanic corrosion behavior of 5050 aluminum alloy. *Mater. Corros.* **67**, 72–83 (2016).
15. Xing, S. H. et al. Effect of dissolved oxygen and coupled resistance on the galvanic corrosion of Cr-Ni low-alloy steel/90-10 cupronickel under simulated deep sea condition. *Mater. Corros.* **68**, 1123–1128 (2017).
16. Tian, H. Y. et al. Combined effect of cathodic potential and sulfur species on calcareous deposition, hydrogen permeation, and hydrogen embrittlement of a low carbon bainite steel in artificial seawater. *Corros. Sci.* **158**, 108089 (2019).
17. Nicolas, A., Mello, A. W. & Sangid, M. D. Relationships between microstructure and micromechanical stresses on local pitting during galvanic corrosion in AA7050. *Corros. Sci.* **154**, 208–225 (2019).
18. Deng, P. et al. Vertical galvanic corrosion of pipeline steel in simulated marine thermocline. *Ocean Eng.* **217**, 107584 (2020).
19. Varma, D. et al. Comparison of galvanic corrosion potential of metal injection molded brackets to that of conventional metal brackets with nickel-titanium and copper nickel-titanium archwire combinations. *J. Contemp. Dent. Pract.* **14**, 488–495 (2013).
20. Wu, W., Cheng, X. Q., Zhao, J. B. & Li, X. G. Benefit of the corrosion product film formed on a new weathering steel containing 3% nickel under marine atmosphere in Maldives. *Corros. Sci.* **165**, 108416 (2020).
21. Yadong, L. I., Qiang, L. I., Tang, X. & Yan, L. I. Reconstruction and characterization of galvanic corrosion behavior of X80 pipeline steel welded joints. *Acta Metallurg. Sin. (Eng. Lett.)* **55**, 801–810 (2019).
22. Huang, C. et al. The galvanic effect of high-strength weathering steel welded joints and its influence on corrosion resistance. *Corros. Eng. Sci. Technol.* **54**, 556–566 (2019).
23. Lu, S. W., Hu, Q., Liu, J. & Huang, F. Parameter optimization for capillary micro-electrode preparation. *J. Wuhan Univ. Sci. Technol.* **42**, 6 (2019).
24. Zhang, Y., Liu, J., Huang, F., Hu, Q. & Lu, S. Effect of composition and size of oxide inclusions on pitting initiation of 2205 duplex stainless steel. *Corros. Sci. Protect. Technol.* **30**, 8 (2018).
25. Liu, P., Han, S. G., Yi, Y. Y. & Yan, C. X. Corrosion behavior of welded joint of Q690 with CMT twin. *Int. J. Corros.* **2018**, 1–9 (2018).
26. Ahmadi, M. & Mirsalehi, S. E. Investigation on microstructure, mechanical properties and corrosion behavior of AISI 316L stainless steel to ASTM A335-P11 low alloy steel dissimilar welding joints. *Mater. High Temp.* **32**, 627–635 (2015).
27. Tian, H. Y. et al. Corrosion evolution and stress corrosion cracking behavior of a low carbon bainite steel in the marine environments: effect of the marine zones. *Corros. Sci.* **206**, 110490 (2022).
28. Professional Standards Compilation Group of People's Republic of China, Corrosion of Metals and Alloys—Alternate Immersion Test in Salt Solution[S]. *China National Standardization Administration* (2018).

29. Zhang, T. Y. et al. Determining on welding methods and parameters for the 3%Ni steel welded joints—insights into the corrosion resistance of the fusion zone. *Mater. Chem. Phys.* **276**, 125365 (2022).
30. Stratmann, M. The investigation of the corrosion properties of metals covered with adsorbed electrolyte layers—a new experimental technique. *Corros. Sci.* **27**, 869 (1987).
31. Ma, Y. T., Li, Y. & Wang, F. H. The atmospheric corrosion kinetics of low carbon steel in a tropical marine environment. *Corros. Sci.* **52**, 1796–1800 (2010).
32. Hao, L., Zhang, S. X., Dong, J. H. & Ke, W. Evolution of corrosion of MnCuP weathering steel submitted to wet/dry cyclic tests in a simulated coastal atmosphere. *Corros. Sci.* **58**, 175–180 (2012).
33. Sun, M. H. et al. Fundamental understanding on the effect of Cr on corrosion resistance of weathering steel in simulated tropical marine atmosphere. *Corros. Sci.* **186**, 109427 (2021).
34. Liu, H. X. et al. Essential role of element Si in corrosion resistance of a bridge steel in chloride atmosphere. *Corros. Sci.* **173**, 108758 (2020).
35. Demoulin, A. et al. The evolution of the corrosion of iron in hydraulic binders analysed from 46- and 260-year-old buildings. *Corros. Sci.* **52**, 3168–3179 (2010).
36. Zhang, T. Y. et al. On how the corrosion behavior and the functions of Cu, Ni and Mo of the weathering steel in environments with different NaCl concentrations. *Corros. Sci.* **192**, 109851 (2021).
37. Nishikata, A., Zhu, Q. J. & Tada, E. Long-term monitoring of atmospheric corrosion at weathering steel bridges by an electrochemical impedance method. *Corros. Sci.* **87**, 80–88 (2014).
38. Bongiorno, V., Gibbon, S., Michailidou, E. & Curioni, M. Exploring the use of machine learning for interpreting electrochemical impedance spectroscopy data: evaluation of the training dataset size. *Corros. Sci.* **198**, 110119 (2022).
39. Wang, Y. et al. Understanding the role of alloyed Cu and P in the initial rust composition of weathering steel formed in a simulated coastal-industrial atmosphere. *Corros. Sci.* **193**, 109912 (2021).
40. Sun, Y. P. et al. The dual nature of Cu content on the corrosion resistance of low alloy steels in sulfuric acid: A time-dependent reversal of corrosion resistance. *Corros. Sci.* **224**, 111486 (2023).
41. Zou, Y., Wang, J. & Zheng, Y. Y. Electrochemical techniques for determining corrosion rate of rusted steel in seawater. *Corros. Sci.* **53**, 208–216 (2011).
42. Zhang, W. H. et al. Corrosion behavior of the low alloy weathering steels coupled with stainless steel in simulated open atmosphere. *Mater. Chem. Phys.* **288**, 126409 (2022).
43. Yang, Y. et al. A study of rust layer of low alloy structural steel containing 0.1% Sb in atmospheric environment of the Yellow Sea in China. *Corros. Sci.* **188**, 109549 (2021).

ACKNOWLEDGEMENTS

This work was supported by the National Natural Science Foundation of China (No. U21A20113) and Major Program (JD) of Hubei Province (2023BAA003).

AUTHOR CONTRIBUTIONS

X.W.: data curation, formal analysis, investigation, methodology, and writing—original draft. F.H.: data curation, investigation, methodology, and writing—review & editing. Q.H.: conceptualization and data curation. J.Z.: sample preparation. J.L.: investigation and supervision.

COMPETING INTERESTS

The authors declare no competing interests.

ADDITIONAL INFORMATION

Correspondence and requests for materials should be addressed to Feng Huang.

Reprints and permission information is available at <http://www.nature.com/reprints>

Publisher's note Springer Nature remains neutral with regard to jurisdictional claims in published maps and institutional affiliations.



Open Access This article is licensed under a Creative Commons Attribution 4.0 International License, which permits use, sharing, adaptation, distribution and reproduction in any medium or format, as long as you give appropriate credit to the original author(s) and the source, provide a link to the Creative Commons license, and indicate if changes were made. The images or other third party material in this article are included in the article's Creative Commons license, unless indicated otherwise in a credit line to the material. If material is not included in the article's Creative Commons license and your intended use is not permitted by statutory regulation or exceeds the permitted use, you will need to obtain permission directly from the copyright holder. To view a copy of this license, visit <http://creativecommons.org/licenses/by/4.0/>.

© The Author(s) 2024, corrected publication 2024